

1 **Quantitative imaging of *Caenorhabditis elegans* dauer larvae during**
2 **cryptobiotic transition using optical diffraction tomography**

3
4 Kyoohyun Kim^{a,b,1}, Vamshidhar R. Gade^{c,d,1}, Teymuraz V. Kurzchalia^{c,2},
5 and Jochen Guck^{a,b,2}

6 ^aBiotechnology Center, Center for Molecular and Cellular Bioengineering, Technische
7 Universität Dresden, 01307 Dresden, Germany

8 ^bMax Planck Institute for the Science of Light & Max-Planck-Zentrum für Physik und
9 Medizin, 91058 Erlangen, Germany

10 ^cMax Planck Institute of Molecular Cell Biology and Genetics, 01307 Dresden, Germany

11 ^dPresent address: Institute of Biochemistry, ETH Zürich, 8093 Zürich, Switzerland

12

13 ¹K.K. and V.G. contributed equally to this work.

14 ²To whom correspondence may be addressed.

15 Email: kurzchalia@mpi-cbg.de or jochen.guck@mpl.mpg.de

16 **Abstract**

17 Upon starvation or overcrowding, the nematode *Caenorhabditis elegans* enters diapause by
18 forming a dauer larva. This larva can further transit into an anhydrobiotic state and survive
19 harsh desiccation. We previously identified the genetic and biochemical pathways essential for
20 survival — but without an accompanying physical model, the mechanistic understanding of this
21 amazing phenomenon will remain inadequate. Neither microscopic investigation of structural
22 changes upon entry into anhydrobiosis nor the most basic quantitative characterization of
23 material properties of living desiccated larvae, however, have been feasible, due to lack of
24 appropriate techniques. Here, we employed optical diffraction tomography (ODT) to
25 quantitatively assess the internal mass density distribution of living larvae in the reproductive
26 and diapause stages. More importantly, ODT allowed for the first time physical analysis of
27 desiccated dauer larvae: their mass density was significantly increased in the anhydrobiotic
28 state. We also applied ODT on different mutants that are sensitive to desiccation. Remarkably,
29 one of them displayed structural abnormalities in the anhydrobiotic stage that could not be
30 observed either by conventional light or electron microscopy. Our advance opens a door to
31 quantitatively assessing fine differences in material properties and structure necessary to fully
32 understanding an organism on the verge of life and death.

33 **Introduction**

34 To withstand fluctuations in environmental conditions, organisms have developed various
35 strategies. One such strategy is entering a dormant state. The extreme form of dormancy is
36 cryptobiosis (hidden life) when the metabolism of an organism under conditions that are not
37 compatible with life (no food, no water or oxygen, very high or low temperatures, high osmotic
38 pressure *etc.*) is reduced to an undetectable level. Upon encountering favorable conditions, the
39 organism exits the cryptobiotic state and resumes metabolism and other vital activities.
40 Prominent examples of cryptobiosis are: survival of dry bacterial or fungal spores, dormant
41 plant seeds, or the ability of tardigrades and some nematodes to survive desiccation (1–4).
42 Studying the molecular, structural, and material mechanisms that accompany this reversible
43 cryptobiotic transition, is fundamental for identifying the essential differences between the
44 living and the dead state of an organism.

45 In the last decade, the nematode *C. elegans* has been established as a model for studying
46 one form of cryptobiosis — anhydrobiosis (life in the absence of water) (5). Under favorable
47 conditions, *C. elegans* goes through the reproductive life cycle where a fertilized egg develops
48 through larval stages from L1 – L4 to a reproductive adult. However, when encountering a
49 harsh environment, overcrowding or food scarcity, *C. elegans* pauses the reproductive cycle
50 and enters diapause by forming a non-feeding dauer larva (6). It has been shown that this dauer
51 larva can survive severe desiccation (5), high osmotic pressure, or freezing (7). The dauer larvae
52 differ from reproductive larvae in both metabolism and morphology (6, 8). They have reduced
53 metabolic activity (oxygen consumption rate, heat production) and as a non-feeding stage, they
54 mostly rely on internal reserves (triacylglycerols) by utilizing glyoxylate shunt to synthesize
55 sugars (8). Morphologically, they differ from reproductive larvae by a significant reduction in
56 volume, which is a result of a radial shrinkage during the formation of the dauer larva.

57 In order to survive harsh desiccation, dauer larvae first need to be exposed to a mild
58 decrease of relative humidity (RH), a process called preconditioning. Previously, we identified

59 genetic and biochemical pathways that are activated during the preconditioning (9) and are
60 crucial for survival. Among these are the many-fold increase of a disaccharide trehalose and
61 massive biosynthesis of an intrinsically disordered protein LEA-1 (5, 9). Despite of this
62 increasing insight into genetic and biochemical details, only very little is known about the actual
63 morphological and material changes that enable the successful survival during reversible
64 transitions. Only some gross anatomical changes, such as a reduction of the overall volume of
65 the worms, have been reported. The detailed structural changes that take place inside the animal
66 have been elusive because it is notoriously difficult to reliably image the process of desiccation
67 or a desiccated worm both with fluorescence and electron microscopy. And going beyond
68 structure, it has not been feasible so far to quantitatively map the distribution of the material
69 properties inside the worm, which accompany, and arguably enable, the amazing transitions
70 between metabolically active and inactive states, between moist and dry, between alive and
71 dead, mainly due to lack of an appropriate non-invasive technique.

72 As a promising solution to address this paucity, optical diffraction tomography (ODT)
73 has recently been developed to quantitatively map the mass density distribution inside
74 biological specimens (10, 11). By employing interferometric microscopy, ODT can determine
75 the three-dimensional (3D) refractive index (RI) distribution of the specimen with diffraction-
76 limited spatial resolution (~ 100 nm). Since RI is roughly isomorphic to electron density, ODT
77 offers an unbiased and label-free view into the structure of living organisms. Moreover, this
78 structure directly translates into quantitative mass density distributions, since RI and density of
79 materials present in biological samples are linearly proportional (12, 13). While ODT has been
80 extensively used for characterizing the mass density distribution inside individual cells (14, 15),
81 its application on larger tissues and whole organisms has hardly been explored.

82 Here, we show that ODT can be employed for imaging the 3D RI distribution in living
83 *C. elegans* larvae with clearly visible morphological features. Reconstructed RI tomograms
84 allowed us to assess the internal mass density distribution, dry mass, and volume of larvae in

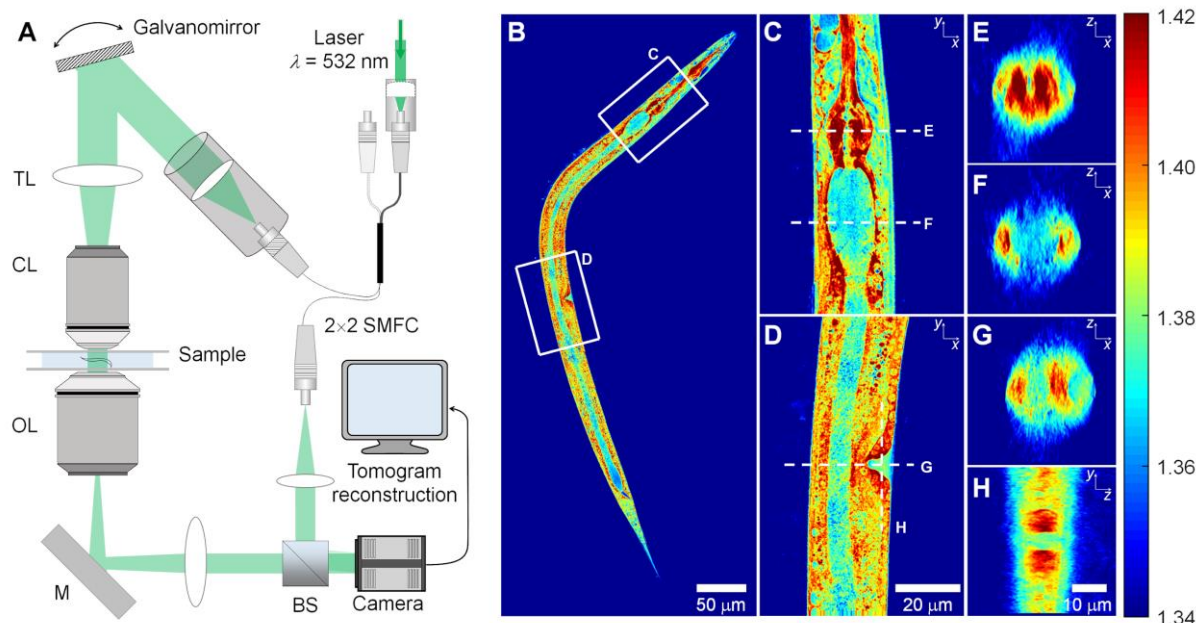
85 the reproductive, diapause and, most importantly, in desiccated stages. The latter gave a unique
86 opportunity to quantify the physical properties of an intact living organism in a desiccated state.
87 We found that the mass density of *C. elegans* larvae increased upon entry into dauer diapause
88 — due to radial volume shrinkage at constant dry mass. Further, the dauer larvae in their
89 anhydrobiotic state exhibited very high RI values ($n \sim 1.5$). This value is comparable to that of
90 glass, and rarely seen in biological objects. The desiccated dauer larvae recovered their original
91 volume in response to rehydration, but with significantly reduced dry mass ($\sim 25\%$) and mass
92 density. We also applied ODT to image several mutants that are sensitive to desiccation.
93 Remarkably, one of them, *lea-1*, showed structural defects in the form of void regions with low
94 mass density, which were not detected by other microscopy techniques. Thus, ODT is able to
95 capture the global as well as detailed local changes of biophysical properties throughout the
96 entire larva. We used this method to quantitatively map the material and structural changes
97 accompanying the anhydrobiotic transition in dauer larvae. Our findings open a door to
98 quantitatively understanding the interdependence of material properties of an organism in
99 relation to growth, diapause and cryptobiotic states.

100 **Results**

101 **Quantitative refractive index and mass density imaging of *C. elegans* larvae**

102 We used optical diffraction tomography (ODT), employing Mach-Zehnder interferometric
103 microscopy (Fig. 1A, see Methods) to image the spatial distribution of refractive index (RI)
104 inside living *C. elegans* larvae. ODT reconstructed the 3D RI distribution of the specimen with
105 diffraction-limited resolution (ca. 120 nm and 440 nm in the lateral and axial direction,
106 respectively) from 2D quantitative phase images obtained from various incident angles. The
107 whole-organism tomogram was enabled by stitching together RI tomograms of multiple fields
108 of view. The mass density was directly calculated from the reconstructed RI tomograms since
109 the RI of most biological samples, n_{sample} , is linearly proportional to the mass density, ρ , as
110 $n_{\text{sample}} = n_{\text{m}} + \alpha\rho$, where n_{m} is the RI of medium and α is the RI increment (dn/dc) with
111 $\alpha = 0.190$ mL/g for proteins and nucleic acids (16, 17).

112 Representative high-resolution images of RI tomograms of a larva at the L3 stage shown
113 in Figure 1B – H and Supplementary Video 1 show that ODT can reveal various morphological
114 structures in the RI contrast. Very clearly distinguishable are pharynx (with metacarpus and
115 terminal bulb) and gut (Fig. 1C and 1E – F). Cells of the latter contain lipid droplets with very
116 high RI, whereas the gut lumen exhibits a much lower RI. Interestingly, the pharynx is a tube
117 formed by very tightly packed muscles, and has a similar RI value to that of lipid droplets. In
118 addition, the vulva, having muscles, exhibits a higher RI than the surrounding tissue (Fig. 1D
119 and 1G – H).



120

121 **Figure 1. Experimental setup and representative 3D RI tomogram of a *C. elegans* larva.**

122 (A) The setup for optical diffraction tomography (ODT). SMFC: single-mode fiber coupler,

123 TL: tube lens, CL: condenser lens, OL: objective lens, M: mirror, and BS: beam splitter. (B)

124 Central cross-sectional slice through a 3D RI tomogram along the x - y plane of a larva at the L3

125 stage, and (C, D) the enlarged cross-sectional RI slices of the pharynx and vulva region

126 indicated in (B). (E, F) Cross-sectional RI slices of (E) pharynx and (F) gut lumen along the x -

127 z plane indicated in (C). (G, H) Cross-sectional RI slices of the vulva region along (G) the x - z

128 plane and (H) y - z plane indicated in (D). Color scale shows RI.

129

130 Next, we set out to investigate the material properties of different larval stages of *C.*

131 *elegans* using ODT. For this we took advantage of the *daf-2(e1370)* strain, which enters the

132 reproductive life cycle (L2, L3 larvae) when exposed to 15°C, but which forms dauer larvae at

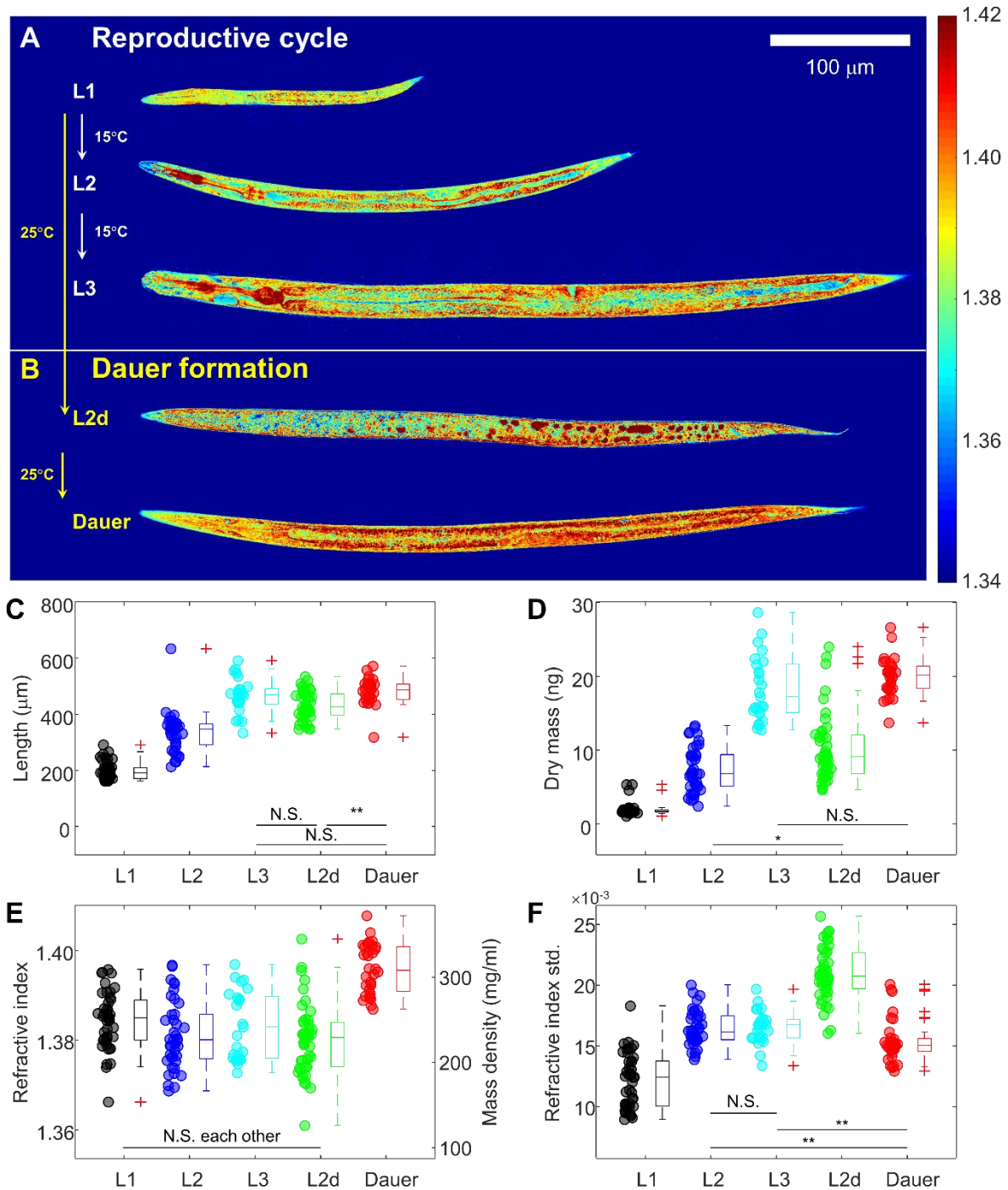
133 25°C via an L2d intermediate (Figure 2A, B). We began with larvae at reproductive larval

134 stages (L1, L2, and L3). The representative RI tomograms in Figure 2A clearly show detailed

135 morphological structures in the larvae. The tomograms also show that the larvae grow in size

136 during the reproductive cycle while maintaining a similar RI value throughout.

137



138

139 **Figure 2. Quantitative physical analysis of *C. elegans* larvae at different larval stages. (A)**

140 Representative central cross-sectional slices through RI tomograms of *C. elegans* larvae at L1,

141 L2, and L3 larval stages in the reproductive cycle. (B) Cross-sectional slices through RI

142 tomograms of *C. elegans* larvae at the L2d and dauer stages. Color scale shows RI. (C – F) The

143 length (C), dry mass (D), mean RI and mass density (E), and standard deviation of RI (F) of *C.*

144 *elegans* larvae at different larval stages. The numbers of larvae measured are $N = 43, 40, 25,$
145 45, and 32 for L1, L2, L3, L2d, and dauer, respectively.

146

147 By quantitative analysis of the reconstructed tomograms, we characterized length, dry
148 mass and mean RI value of the larvae (see Methods). As expected, both length and dry mass
149 increased during growth from L1 to L3 (Fig. 2C, D). Importantly, however, the mean RI value
150 and therefore the mean mass density of the larvae did not change significantly ($1.3845 \pm 0.0020,$
151 $1.3812 \pm 0.0024,$ and 1.3835 ± 0.0032 at L1, L2, and L3 stage, respectively; corresponding to
152 the mass density of 249.8 ± 10.4 mg/ml, 232.4 ± 12.7 mg/ml and 244.9 ± 16.6 mg/ml; Figure
153 2E). These measurements indicate the presence of regulatory mechanisms coordinating the
154 biosynthesis of different classes of molecules required for growth and maintenance of
155 metabolism and structure of cells. Moreover, the standard deviation of RI inside individual
156 larvae at the L1 stage was as low as 0.0120 ± 0.0007 and increased to 0.0164 ± 0.0005 and
157 0.0165 ± 0.0006 at the L2 and L3 stages, respectively (Fig. 2F). The increasing heterogeneity
158 of RI and mass density quantifies the developmental growth and maturation of organs such as
159 pharynx (with metacarpus and terminal bulb) and gut.

160

161 **Dauer larvae have higher mass density than larvae in the reproductive cycle**

162 As a next step, we investigated the RI distribution during the transition into diapause. As shown
163 in Figure 2B and 2E, the pre-dauer larval stage called L2d larvae exhibited a similar average
164 RI value (1.3802 ± 0.0024) to that of larvae in the reproductive cycle. However, the dauer larvae
165 showed significantly higher RI values (1.3960 ± 0.0020). The increased RI, and mass density,
166 of the dauer larvae might correlate with both radial shrinkage and increased accumulation of
167 lipid droplets, known to occur during the transition to diapause. We estimated to which extent
168 the accumulation of lipid droplets contributes to the increase in RI and mass density. For this,
169 we correlated the RI tomograms with epi-fluorescence images of dauer larvae stained with Nile

170 Red for lipid droplets in the same optical setup (see Methods, Supplementary Fig. 1A, B). The
171 mean RI value of the regions containing lipid droplets was 1.4184 ± 0.0025 , which is higher
172 than non-lipid regions with 1.4081 ± 0.0010 (Supplementary Fig. 1C). In addition, the mean RI
173 value of non-lipid regions by itself was already significantly higher than that of the L3 larvae
174 in the reproductive cycle. Altogether our findings suggest that the increased RI in the dauer
175 larva originates from both volume shrinkage and lipid droplet accumulation. The first increases
176 the overall RI and mass density, whereas the latter contributes to the additional RI increase.

177

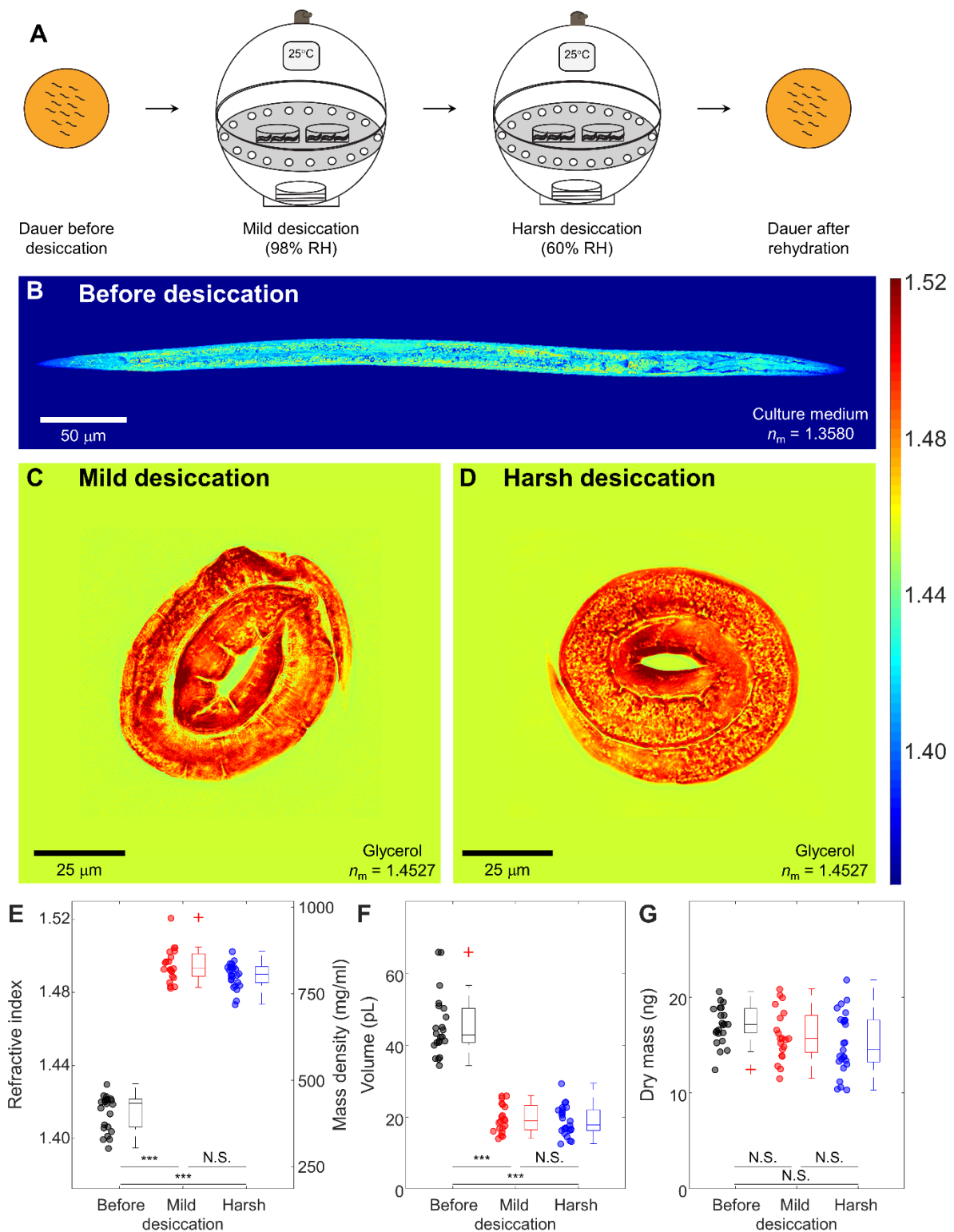
178 **Entry into anhydrobiotic state increases RI and mass density of dauer larvae dramatically**

179 The most interesting findings were revealed in the investigation of morphological and
180 biophysical changes in dauer larvae in a desiccated state. As previously described (5) dauer
181 larvae need to be preconditioned (mild desiccation at 98% RH) to survive harsh desiccation
182 (60% RH; see Figure 3A). In the process, the larvae lose up to 80% and over 95% of their body
183 water, respectively. As shown in Figure 3B – D, after desiccation the RI of dauer larvae
184 displayed surprisingly high RI values: after preconditioning the mean RI was 1.4955 ± 0.0043
185 and after harsh desiccation 1.4899 ± 0.0028 , respectively (Figure 3E). The increase in RI was
186 so high that to reduce the mismatch between the larvae and the surrounding medium, we
187 immersed the desiccated larvae into glycerol as an imaging medium ($n = 1.4527$). The
188 significant increase of the mean RI in the desiccated dauer larvae was mainly due to the about
189 2.3 to 2.4-fold decrease in volume (Figure 3F). In contrast, the dry mass of the dauer larvae
190 decreased only slightly from 17.1 ± 0.9 ng to 16.1 ± 1.2 ng and 15.2 ± 1.3 ng (Figure 3G).

191 Most cells and tissues display RI values ranging from 1.35 to 1.39 (18). Reported
192 exceptions are diatoms whose cell walls are made of silica glass that has a high RI value of 1.46
193 and the basalia spicules of some glass sponges, which can reach RI values of 1.48 in their core
194 (19, 20). Remarkably, desiccated dauer larvae had an average RI of almost 1.50 (Figure 3D),
195 with some internal regions reaching 1.52 (Figure 3C, D), considerably higher than anything

196 reported for other biological specimens. Thus, desiccated larvae have optical properties similar
197 to that of glass, and quite unlike living matter. This, together with the transition of the cytoplasm
198 from a liquid to a solid-like state (due to loss of 95% of body water), seem to be physical
199 measures of the fact that desiccated *C. elegans* larvae are indistinguishable from dead objects.

200



201

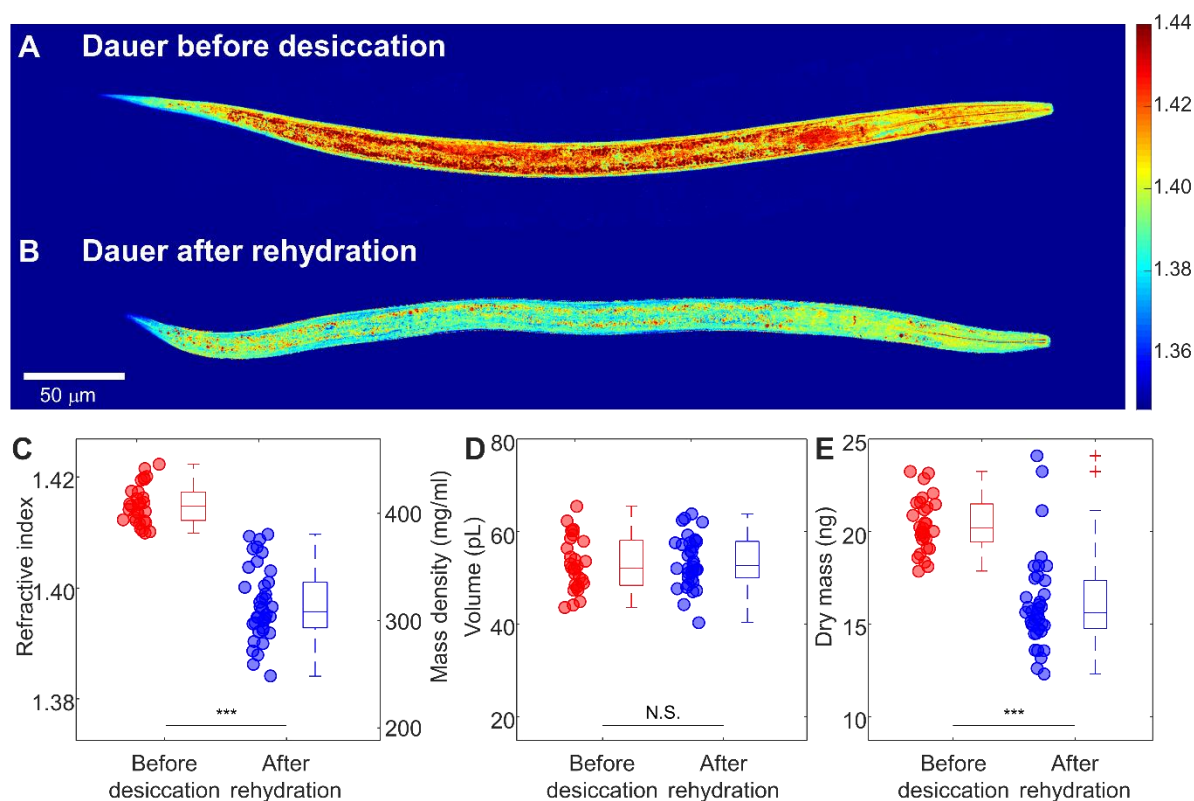
202 **Figure 3. Quantitative ODT analysis of desiccated dauer larvae.** (A) Schematic diagram for

203 preparing *C. elegans* dauer larvae by consecutive mild (98% relative humidity, RH) and harsh

204 desiccation (60% RH). (B) Central cross-sectional slice through RI tomogram of a typical *C.*

205 *elegans* dauer larva (similar to Figure 2B, but with different RI scale). (C – D) Representative
206 cross-sectional slices through RI tomograms of desiccated dauer larvae after (C) mild (98%
207 RH) and (D) harsh (60% RH) desiccation. Color scale shows RI. (E – G) Mean RI (E), volume
208 (F), and dry mass (G) of *C. elegans* dauer larvae in different desiccated stages. The numbers of
209 desiccated larvae measured are $N = 22, 20,$ and 25 for dauer, mild and harsh desiccated state,
210 respectively.

211
212 Upon rehydration with water, the desiccated dauer larvae can revive within a few hours
213 (5) and can develop further into reproductive adults under optimum conditions. As desiccation
214 followed by rehydration induces breakdown of several biomolecules (*e.g.*, triacylglycerols and
215 trehalose) (5, 8), we hypothesized that the rehydrated dauer larvae might have different RI
216 values and dry mass in comparison to the dauer larvae before desiccation. As shown in Figure
217 4A, B for typical RI tomograms and Figure 4C for quantitative results, the rehydrated dauer
218 larvae had a mean RI value of 1.3971 ± 0.0022 , which was significantly lower than that of the
219 dauer larvae before desiccation with 1.4150 ± 0.0013 . The rehydrated dauer larvae recovered
220 the volume of dauers before desiccation (53.0 ± 2.2 pL and 55.5 ± 3.3 pL, respectively; Figure
221 4D). Interestingly, the dry mass of the dauer larvae decreased by almost 25% from 20.4 ± 0.6
222 ng before desiccation to 16.1 ± 0.8 ng after rehydration (Figure 4E). This result quantitatively
223 confirms our previous findings that the dauer larvae consume significant amounts of
224 triacylglycerols and trehalose during desiccation and rehydration — they metabolize a quarter
225 of their own internal contents in the process.



226

227 **Figure 4. Quantitative ODT analysis of dauer larvae before desiccation and after**

228 **rehydration.** (A, B) Central cross-sectional slices of RI tomograms of typical *C. elegans* dauer

229 larvae (A) before desiccation and (B) after rehydration. Color scale shows RI. (C – E) Mean RI

230 and mass density (D), volume (E), and dry mass (F) of *C. elegans* dauer larvae before

231 desiccation and after rehydration. The numbers of dauer larvae measured are $N = 29$ and 38 ,

232 respectively.

233

234 **ODT reveals structural differences in desiccation-sensitive mutants**

235 Previous studies have shown that *C. elegans* dauer larvae activate several biochemical pathways

236 to survive harsh desiccation (9). One of them leads to massive biosynthesis of the disaccharide

237 trehalose, which is involved in protecting phospholipid bilayers against water-induced damage

238 during rehydration (5). Another essential factor for survival is biosynthesis of an intrinsically

239 disordered protein LEA-1 (late embryogenesis abundant) (7, 9). Deletion mutants with the

240 biosynthetic pathways of trehalose (double mutant lacking biosynthetic enzymes TPS-1 and

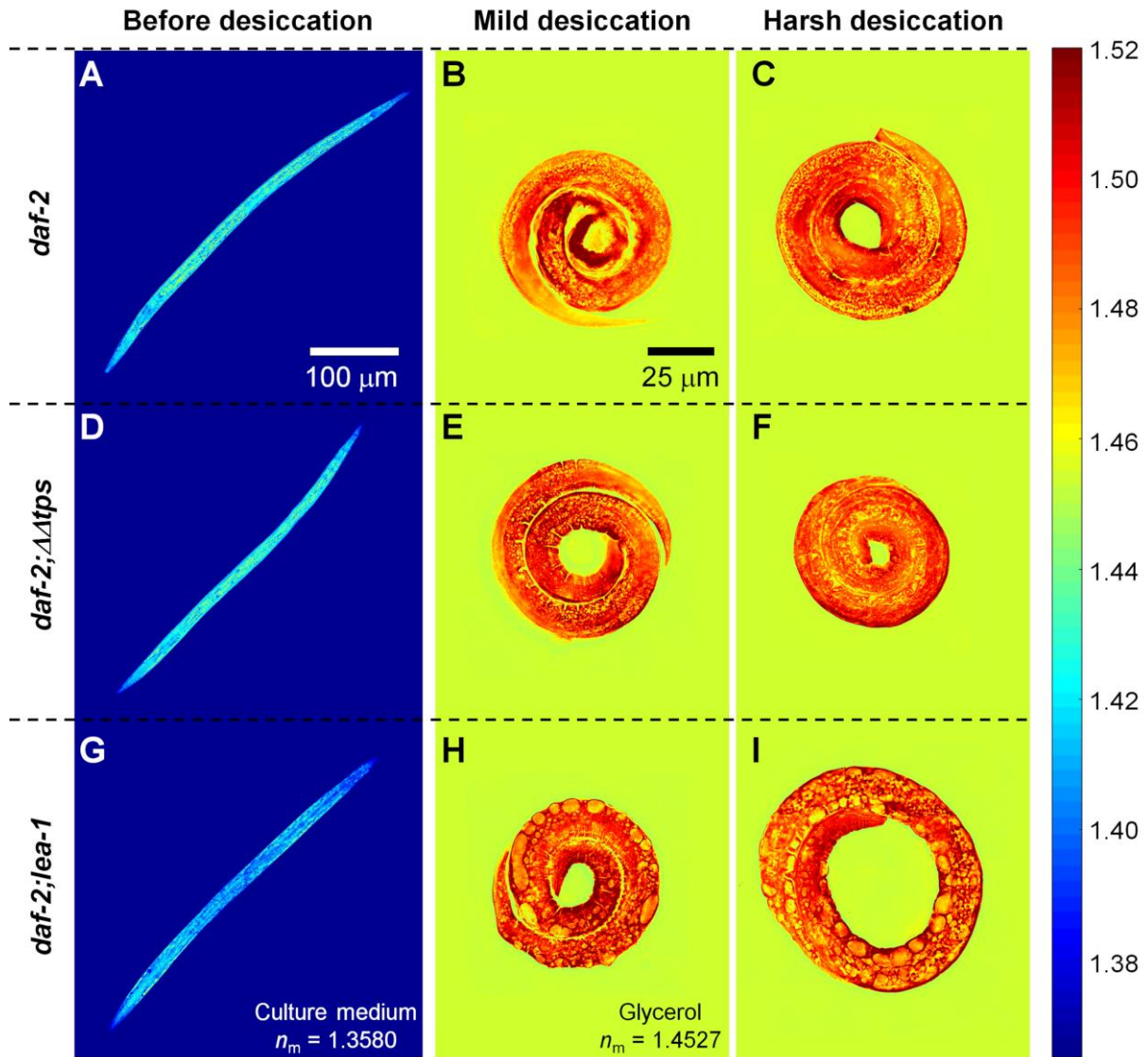
241 TPS-2, *daf-2;ΔΔtps*) or of LEA-1 (*daf-2;lea-1*) abolished are non-viable after rehydration (7).
242 Thus, we investigated how deficiency in trehalose and LEA-1 in these mutants influences the
243 physical characteristics of desiccated dauer larvae. Is there a correlation between the latter and
244 the viability of larvae?

245 As shown in Figure 5 and Supplementary Video 2 – 4 for the representative ODTs and
246 Supplementary Fig. 2A for the quantitative analysis, the trehalose and LEA-1 deletions did not
247 affect overall mean RI value and mass density significantly — neither before nor after mild and
248 harsh desiccation. Only the dauer larvae of the *lea-1* deletion mutant had a slightly lower mean
249 RI value than wild type dauer larvae. Not surprising for mutants that cannot produce trehalose,
250 the volume and dry mass of the dauer larvae before and during desiccation were lower than that
251 of control dauer larvae in the same conditions (Figure 5D – F and Supplementary Fig. 2B, C).
252 The result is consistent with previous studies showing that trehalose is produced largely during
253 the preconditioning (5) However, since volume and mass changes in the trehalose mutants
254 scaled proportionally, the overall densities of wild type and both mutant larvae were similar in
255 the anhydrobiotic state.

256 Even though the *lea-1* mutants were inconspicuous in their overall physical properties,
257 they displayed very interesting internal structural anomalies. As seen in Figs. 5H-I, the RI
258 tomograms of desiccated dauer larvae of the *lea-1* deletion mutant displayed distinct void
259 regions with significantly lower RI value. By visual inspection, the void regions corresponded
260 to mid gut regions anatomically. This finding based on ODT measurements quantifies
261 morphological and physicochemical differences in desiccated samples that are hardly, or not at
262 all revealed by light or electron microscopy (EM). As seen in Supplementary Fig. 3, bright field
263 microscopy did not display any difference in contrast to wild type. Differential interference
264 contrast (DIC) microscopy did show circular structures that might correspond to the void
265 volumes detected by ODT. But without the 3D imaging and quantification capabilities of ODT,
266 one cannot determine these differences in local material properties with certainty. Further,

267 imaging with ODT has considerable advantages to EM stemming from the fact that it can image
268 specimens in their native state and without any preparative steps, as in EM, that are necessarily
269 destructive and also bear the danger of creating artifacts or eliminating differences. It must be
270 said that EM principally does not allow the analysis of a desiccated worm as it can only be
271 applied to samples after rehydration. The electron micrographs of the dauer larvae of *lea-1*
272 deletion mutant after harsh desiccation, and subsequently necessary rehydration, show that the
273 annular morphology of the desiccated larvae is distorted (Supplementary Fig. 4). This
274 observation can, however, only indirectly indicate possible structural changes of *lea-1* dauer
275 larvae in the desiccated state.

276 The measured RI tomograms were further analyzed quantitatively to investigate the
277 mass density difference in void regions. The void regions were segmented from the RI
278 tomograms by applying the Otsu method (21), and the mean RI value of the void regions and
279 peripheral regions was quantified. The periphery of the void regions was segmented by dilating
280 the binary masks for the void regions by 5 μm . The mean RI value of the void regions of the
281 dauer larvae in mild and harsh desiccation conditions was 1.4686 ± 0.0004 and 1.4686 ± 0.0006 ,
282 respectively, which were significantly lower than the peripheral regions with 1.4962 ± 0.0006
283 and 1.4972 ± 0.0008 (Supplementary Fig. 5). The relative RI difference suggests that the void
284 region is 18% less dense than peripheral regions. It is remarkable that ODT can detect and
285 quantitate such fine structural differences in an organism. Altogether our ODT-based findings
286 shed light onto the correlation between material and structural properties of an organism and
287 its survival ability in extreme environments.



288

289 **Figure 5. ODT analysis of desiccated dauer larvae with different genetic mutations.**

290 Typical central cross-sectional slices through RI tomograms of *C. elegans* dauer larvae of (A –

291 C) controls, (D – F) trehalose deletion mutants *daf-2;ΔΔtps*, and (G – I) *lea-1* deletion mutants

292 *daf-2;lea-1*, respectively. (A, D, G) represent dauer larvae before, (B, E, H) after mild (98%

293 RH), and (C, F, I) after harsh desiccation (60% RH). Color scale shows RI.

294 **Discussion**

295 In this study, we employed ODT to reconstruct the 3D RI distribution of *C. elegans* larvae in
296 reproductive stages and dauer diapause. From these RI tomograms, the physical properties
297 including mass density, volume, and dry mass were quantitatively analyzed. So far, ODT has
298 mostly been applied for single-cell analysis mainly due to the limited field-of-view (14, 15),
299 and few studies briefly visualized the RI tomograms of *C. elegans* (22, 23). This study is the
300 first quantitative ODT analysis of an entire organism.

301 We used ODT to provide the biophysical and structural properties of live dauer larvae,
302 which have not been charted by conventional microscopic techniques. Previously, EM had been
303 used to reveal the fine structures of dauer larvae and their density differences under harsh
304 desiccation conditions with its typical very high spatial resolution (5, 24). However, the sample
305 preparation for desiccated dauer larvae requires rehydrating the larvae for a brief time before
306 further processing. Thus, EM images we obtain do not depict larvae in desiccated state but
307 rather changes that occur after first desiccation and then subsequent rehydration. ODT might
308 not provide the same spatial resolution as EM, but it can quantitatively assess structure and
309 physical properties of intact dauer larvae without any sample preparation steps. In principle,
310 ODT can even trace the changes within the same larvae during development and the desiccation
311 process. As another relevant light microscopy, fluorescence microscopy provides molecularly
312 specific localization of fluorescently stained proteins and organelles in live dauer larvae.
313 However, fluorescence imaging is susceptible to phototoxicity and can only visualize molecules
314 labeled selectively. It is not suitable to quantify physical properties and their changes. In
315 contrast, ODT allows revealing the mass density of overall unbiased substances in the entire
316 organism. Since *C. elegans* larvae can be considered optically transparent, at least up to the L3
317 stage in the reproductive life cycle (25), the first-order Rytov approximation is still valid for
318 reconstructing RI tomograms. To extend analysis to even larger and optically denser specimens,
319 various computational algorithms for tomogram reconstruction have recently been developed

320 to take into account multiple photon scattering in the sample (23, 26). Employing such
321 algorithms, we can extend our studies in the future also to L4 larvae and adult *C. elegans* worms.

322 From reconstructed RI tomograms, we found that the *C. elegans* larvae in the
323 reproductive cycle maintain a constant mass density during development, while entry to dauer
324 diapause increases the mass density significantly. From the correlation between the RI
325 tomograms and epi-fluorescence images of Nile Red-stained lipid droplets, we conclude that
326 the increased mass density in dauer larvae is presumably due to this lipid droplet accumulation,
327 in addition to the radial shrinkage they undergo during dauer formation. This hypothesis can be
328 tested by analyzing whether mutant strains that do not undergo proper radial shrinkage (24, 27)
329 or that deplete lipid droplets rapidly (28) exhibit a similar increase in mass density.

330 Biophysical properties of organisms that can survive extreme environments have until
331 now only sporadically been studied. One remarkable finding of our study is that dauer larvae
332 in their anhydrobiotic state (where most of the body water is lost) have a very high RI value
333 reaching $n \sim 1.5$. This RI value is usually not found in biological specimens and is comparable
334 to that of glass (Supplementary Fig. 6). While this finding needs further investigation into the
335 biological relevance of why and how desiccated dauer larvae acquire such high RI and mass
336 density, one can speculate that the increased mass density also corresponds to altered
337 mechanical properties. A recent study showed that crowding above the critical mass density (\sim
338 340 mg/ml) induces glass-forming behavior of the cytoplasm in cells with a resulting increased
339 viscosity (29). This mass density value corresponds to an RI value of about 1.4, which ranges
340 between that of dauer larvae and desiccated dauer larvae as found in our study. Moreover, it
341 has been shown that the viscoelastic property of tardigrades, one of the other species that can
342 enter an anhydrobiotic state, becomes glass-like in desiccation (30). Therefore, the dramatic
343 increase in RI and mass density may reflect a glass transition of the cytoplasm during
344 desiccation. It is conceivable that such a transition contributes to an increased mechanical
345 stability in the desiccated state of the organism. This hypothesis needs further validation by

346 direct measurements of mechanical properties of desiccated dauer larvae. Conventional,
347 contact-based techniques for mechanical phenotyping of biological samples with (sub-)cellular
348 resolution, such as atomic force microscopy-enabled nanoindentation, necessitate a destruction
349 and slicing of the sample in order to gain access to internal material properties (31). This
350 approach would be inappropriate to obtain reliable mechanical information about the process
351 of desiccation. However, recently, non-invasive microscopic techniques to probe the
352 mechanical properties of biological samples directly inside living biological samples have
353 emerged, including Brillouin microscopy (32–35) and time-lapse quantitative phase
354 microscopy (36, 37). Combining ODT with such microscopic techniques can in the future
355 provide decisive information on the detailed nature of the material transitions during dauer
356 formation and desiccation of *C. elegans* larvae.

357 Our measurements on rehydrated dauer larvae revealed that the dry mass is significantly
358 decreased (~ 25%) in rehydrated larvae while their volume remains constant. It is worth noting
359 that ODT provides absolute and unbiased quantification of how much material the larvae
360 consume during the rehydration process. In accordance with our previous results, we found that
361 the degradation of essential biomolecules (triacylglycerols, trehalose) upon desiccation and
362 rehydration (5, 8) manifest on the dry mass content of the dauer larvae. The significant increase
363 and decrease of mass density during harsh desiccation and rehydration without damage draw
364 our attention to the connection between biochemical pathways and material properties of the
365 larvae in such dramatic transitions. Hence, we quantitatively characterized the physical
366 differences of deletion mutants that do not survive desiccation. To the best of our knowledge,
367 this is the first study reporting the overall changes in the RI and mass density distributions of
368 an entire multicellular organism with genetic mutations. The mean RI value of the deletion
369 mutants remained the same as the wild type desiccated larvae. However, we observed a
370 decreased dry mass and void regions with low mass density in deletion mutants. The trehalose
371 deletion mutant (*daf-2;ΔAtps*) displayed a decreased dry mass, which is in accordance with our

372 previous observation that trehalose levels are normally accumulated during desiccation (5). The
373 *lea-1* deletion mutant larvae showed distinct structural differences in the RI distribution during
374 desiccation, as they exhibited void regions with significantly lower RI value in the RI
375 tomograms. The molecular mechanism of how LEA-1 confers desiccation tolerance to dauer
376 larvae remains elusive. Several *in vitro* studies have indicated that LEA-1 is involved in the
377 prevention of protein aggregation during desiccation (38, 39). In combination with our electron
378 microscopy results, the structural defects in the RI tomograms of *lea-1* deletion mutant indicate
379 that LEA-1 might maintain the functionality of cytosolic proteins which further assist in the
380 maintenance of the annular morphology of the desiccated larvae (Supplementary Fig. 4).
381 Further correlative investigations with fluorescently tagged LEA-1 in wild type larvae and
382 corresponding regions in *lea-1* deletion mutant should lead towards the precise mechanism.

383 To conclude, we utilized ODT to quantitatively investigate the physical and structural
384 changes in a living *C. elegans* larvae during dauer formation and upon desiccation. We revealed
385 that the RI of dauer larvae is higher than that of larvae in the reproductive cycle, and becomes
386 even as high as the RI of glass ($n \sim 1.5$) in the desiccated state. Moreover, dauer larvae of the
387 deletion mutants of trehalose and LEA-1 exhibited distinct morphological changes in the
388 desiccation condition, which may affect the survival in such harsh environments. The biological
389 relevance of a higher mass density of the larvae during dauer formation and upon desiccation
390 requires further investigation. However, the physical understanding and corresponding
391 quantitative modeling of cryptobiotic transitions in *C. elegans* larvae can now be based on
392 actual physical parameters determined by methods such as ODT. As such, our study paves the
393 way to a more complete understanding of the underlying mechanisms to sustain the integrity of
394 nematodes, and ultimately other organisms, in transitions between life and death.

395 **Methods**

396 **Materials, *C. elegans* strains and growth conditions**

397 The Caenorhabditis Genetic Centre (CGC) provided the *C. elegans* strain *daf-2(e1370)* and the
398 *E. coli* strain NA22. The compound mutant strains of *daf-2(e1370)III;lea-1(tag1676)V*, *tps-*
399 *2(ok526)II*; *daf-2(e1370)III*; *tps-1(ok373)X(daf-2;ddtps)* were generated during our previous
400 studies (5, 7).

401 *daf-2(e1370)* eggs were incubated in 1X M9 buffer for a few hours at room temperature
402 at shaking to obtain synchronized hatched L1 larvae. These L1 larvae were plated on NGM
403 agar plates with *E. coli* NA22. Half of the plates were incubated at 15°C and the rest at 25°C
404 for reproductive and dauer larvae formation, respectively. Larval stages were monitored,
405 visually confirmed for respective stages, and collected from the plate.

406

407 **Desiccation of *C. elegans* dauer larvae**

408 Larvae at various stages were collected in water and washed twice with water to remove any
409 debris. For preparing preconditioned and desiccated larvae, a dauer suspension of 5 µl was
410 pipetted onto a coverslip (VWR International) and exposed to 98% RH (relative humidity) for
411 4 days and 60% RH for 1 day subsequently. For imaging desiccated dauer larvae, the dauer
412 larvae were immersed in glycerol ($n = 1.4527$) in order to reduce the RI difference between
413 dauer larvae and the surrounding medium. The RI of the medium was measured using an Abbe
414 refractometer (2WAJ, Arcarda GmbH). For imaging rehydrated larvae after desiccation, the
415 dauer larvae were rehydrated for 2 hours with water and then anesthetized with levamisole
416 (Sigma) prior to imaging.

417

418 **Optical setup for optical diffraction tomography**

419 The three-dimensional (3D) refractive index (RI) distribution of *C. elegans* larvae was
420 determined using optical diffraction tomography (ODT). The optical setup was described

421 previously (40). Briefly, ODT employs Mach-Zehnder interferometry to measure multiple
422 complex optical fields from various incident angles (Figure 1C). A laser beam ($\lambda = 532$ nm,
423 frequency-doubled Nd-YAG laser, Torus, Laser Quantum Inc.) was coupled into an optical
424 fiber and divided into two paths using a 2×2 single-mode fiber-optic coupler (TW560R2F2,
425 Thorlabs). One beam was used as a reference beam and the other beam passed through a tube
426 lens ($f = 175$ mm) and a water-dipping objective lens (NA = 1.0, 40 \times , Carl Zeiss AG) to
427 illuminate the sample on the stage of a home-built inverted microscope. The beam diffracted
428 by the sample was collected with a high numerical-aperture objective lens (NA = 1.2, 63 \times ,
429 water immersion, Carl Zeiss AG) and a tube lens ($f = 200$ mm). To reconstruct a 3D RI
430 tomogram of the sample, the sample was illuminated from 150 different incident angles scanned
431 by a dual-axis galvano-mirror (GVS012/M, Thorlabs Inc.) located in the conjugate plane of the
432 sample. The diffracted beam interfered with the reference beam at an image plane, and
433 generated a spatially modulated hologram, which was recorded with a CCD camera (FL3-U3-
434 13Y3M-C, FLIR Systems, Inc.). The total magnification of the setup was 57 \times , and the field-of-
435 view (FOV) of the camera covers $86.2 \mu\text{m} \times 86.2 \mu\text{m}$.

436

437 **Tomogram reconstruction and quantitative analysis**

438 The complex optical fields of light scattered by the samples were retrieved from the recorded
439 holograms by applying a Fourier transform-based field retrieval algorithm (41). To measure the
440 3D RI tomograms of whole larvae and desiccated dauers, whose size is much larger than the
441 FOV, segmented complex optical fields of the samples were measured and digitally stitched by
442 a custom-made MATLAB script. The 3D RI distribution of the samples was reconstructed from
443 the retrieved complex optical fields via the Fourier diffraction theorem, employing the first-
444 order Rytov approximation (10, 42). A more detailed description of tomogram reconstruction
445 can be found elsewhere (43).

446 On the reconstructed tomograms, Otsu's thresholding method (21) was used to segment
447 the region occupied by the larvae from the background, and quantitative analysis was performed
448 to calculate mean RI value, dry mass, volume, and the standard deviation of RI in the individual
449 larvae. The mass density of the larvae was directly calculated from the mean RI value, since
450 the RI value in biological samples, $n(x,y,z)$, is linearly proportional to the mass density of the
451 material, $\rho(x,y,z)$, as $n(x,y,z) = n_m + \alpha\rho(x,y,z)$, where n_m is the RI value of the surrounding
452 medium and α is the RI increment (dn/dc) with $\alpha = 0.190$ mL/g for proteins and nucleic acids
453 (16, 17). The RI of the medium was measured using an Abbe refractometer (2WAJ, Arcarda
454 GmbH). The volume of the larvae was extracted by counting the number of voxels in the
455 segmented region and the dry mass of the larvae was calculated by integrating the mass density
456 inside the segmented region. All tomogram acquisition and data analysis were performed using
457 custom-written MATLAB scripts (R2018b, MathWorks, Inc.), which are available upon
458 request. Tomogram rendering was performed by an open-source software (tomviz 1.9.0,
459 <https://tomviz.org/>). The RI tomograms of all larvae presented in the current study are available
460 from figshare under the following link: <https://doi.org/10.6084/m9.figshare.14483331>.

461

462 **Electron microscopy of desiccated dauer larvae**

463 *daf-2* and *daf-2*; *lea-1* dauers that were non-preconditioned, preconditioned (98%RH) and
464 desiccated (60%RH) were rehydrated with distilled water for 20 min after which water was
465 soaked off and bovine serum albumin solution was added. These dauer samples were then
466 transferred to carriers of 3 mm diameter and 0.1 mm depth and rapidly frozen in a high-pressure
467 freezing machine (Leica, EM ICE). For automated freeze substitution, frozen samples from the
468 above step were transferred into vials containing a special freeze substitution cocktail (Acetone,
469 1% Osmium tetroxide, 0.1% Uranyl acetate) by increasing the temperature to 4.5°C. After
470 thawing, samples were rinsed with acetone to remove any freeze substitution cocktail. Then the
471 samples were infiltrated with Epon LX112 resin: Acetone solution (1:2, 1:1, 2:3) for 1.15 h,

472 1.30 h, 2 h respectively. Finally, they were left in pure resin overnight and then for 4 h. After
473 polymerization and embedding, sections of 70 nm thickness were taken with an ultramicrotome
474 (Leica, UCT) and these sections were incubated in 1% Uranyl acetate in 70% methanol for ten
475 minutes, followed by several washes in 70% methanol, 50% methanol, 30% methanol and
476 finally with distilled water. Sections were further incubated in Lead citrate for 5 minutes,
477 followed by washes with distilled water. Sample sections were analysed with an electron
478 microscope (Tecnai12, Philips) and images were acquired with TVIPS camera (Tietz).

479

480 **Lipid droplet staining and imaging**

481 *daf-2(e1370)* eggs were plated on NGM agar plates with *E. coli* NA22 mixed with Nile Red
482 (Thermo scientific, 200 µg/ml). These plates were incubated at 25°C for dauer formation. After
483 three days, dauer formation was visually confirmed. Dauer larvae were collected from the
484 plates, washed thrice with water at 1500 g for 1 min to remove any debris and excess dye
485 adhering to the larvae. The dauer larvae were anaesthetized with levamisole (Sigma) and
486 imaged.

487 Fluorescence emission intensity of Nile red-stained dauer larvae was measured by epi-
488 fluorescence microscopy combined in the same optical setup as ODT. The detailed
489 configuration was described elsewhere (44). The incoherent light from a halogen lamp (DC-
490 950, Dolan-Jenner Industries Inc.) was passed through a bandpass filter (bandwidth $\lambda = 545 \pm$
491 25 nm, Carl Zeiss AG), and coupled into the same beam path in the ODT using a three-channel
492 dichroic mirror (FF409/493/596-Di01-25×36, Semrock Inc.). The fluorescence emission signal
493 from Nile Red in lipid droplets was collected by the same objective lens and acquired using the
494 ODT camera. A bandpass filter (bandwidth $\lambda = 605 \pm 70$ nm, Carl Zeiss AG) was placed in
495 front of the camera to suppress the excitation beam. The lipid regions were segmented from
496 measured epi-fluorescence images by applying Otsu's thresholding method and correlated with

497 the cross-sectional slices of RI tomograms, from which the mean RI values of lipid and non-
498 lipid regions were calculated.

499

500 **Statistical Analysis**

501 Measured quantities were reported as mean \pm standard error of mean (SEM) throughout.

502 Statistical significance was determined using Mann-Whitney U test. The shown asterisks

503 indicate the statistical significance as * $p < 0.01$, ** $p < 0.001$, and *** $p < 0.0001$, respectively.

504

505 **Acknowledgements**

506 The authors acknowledge financial support from the Volkswagen Foundation (Life? research

507 grant 92847). We thank Vasily Zaburdaev, Simon Alberti, Gheorghe Cojoc, Raimund

508 Schlüßler, Titus M. Franzmann, Hui-Shun Kuan, Shada Abuhattum, and Anne Eßlinger for

509 helpful discussions. We thank Daniela Vorkel from the electron microscopy facility of MPI-

510 CBG for technical assistance.

511

512 **Author contributions**

513 KK conducted the ODT measurements and analyzed the data; VG prepared the *C. elegans*

514 larvae; KK and VG interpreted the ODT data; KK, VG, TK, and JG contributed to the

515 conception and design of the study and interpretation of the results, and wrote the manuscript.

516 **References**

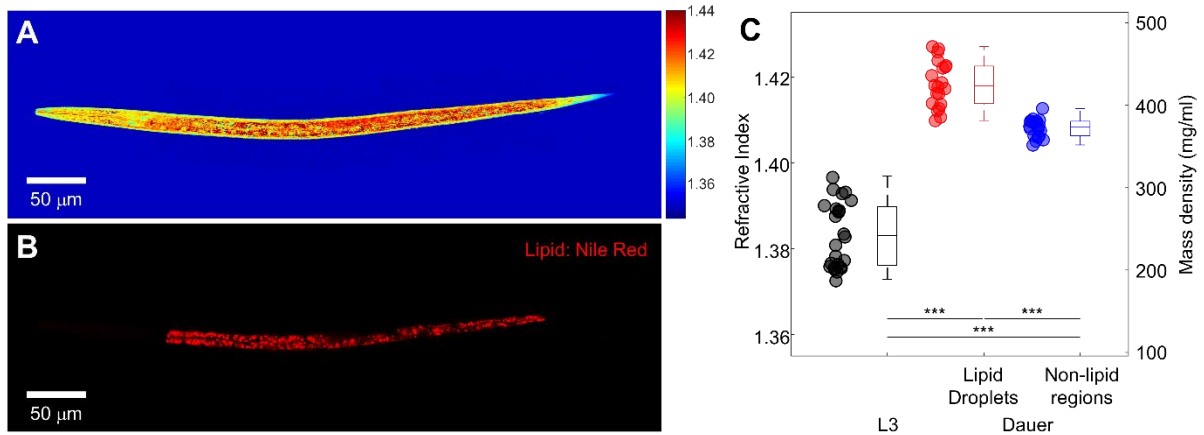
- 517 1. I. E. Young, P. C. Fitz-James, Chemical and Morphological Studies of Bacterial Spore
518 Formation. *J. Biophys. Biochem. Cytol.* **6**, 467–482 (1959).
- 519 2. V. W. Cochrane, Dormancy in Spores of Fungi. *Trans. Am. Microsc. Soc.* **93**, 599 (1974).
- 520 3. J. D. Bewley, Seed Germination and Dormancy. *Plant Cell* **9**, 1055–1066 (1997).
- 521 4. R. I. Sommerville, K. G. Davey, Diapause in parasitic nematodes: a review. *Can. J. Zool.*
522 **80**, 1817–1840 (2002).
- 523 5. C. Erkut, *et al.*, Trehalose renders the dauer larva of *Caenorhabditis elegans* resistant to
524 extreme desiccation. *Curr. Biol.* **21**, 1331–1336 (2011).
- 525 6. J. W. Golden, D. L. Riddle, The *Caenorhabditis elegans* dauer larva: Developmental
526 effects of pheromone, food, and temperature. *Dev. Biol.* **102**, 368–378 (1984).
- 527 7. V. R. Gade, S. Traikov, J. Oertel, K. Fahmy, T. V. Kurzchalia, *C. elegans* possess a
528 general program to enter cryptobiosis that allows dauer larvae to survive different kinds
529 of abiotic stress. *Sci. Rep.* **10**, 13466 (2020).
- 530 8. C. Erkut, V. R. Gade, S. Laxman, T. V. Kurzchalia, The glyoxylate shunt is essential for
531 desiccation tolerance in *C. elegans* and budding yeast. *Elife* **5**, e13614 (2016).
- 532 9. C. Erkut, *et al.*, Molecular Strategies of the *Caenorhabditis elegans* Dauer Larva to
533 Survive Extreme Desiccation. *PLoS One* **8**, e82473 (2013).
- 534 10. Y. Sung, *et al.*, Optical diffraction tomography for high resolution live cell imaging. *Opt.*
535 *Express* **17**, 266–277 (2009).
- 536 11. Y. Park, C. Depeursinge, G. Popescu, Quantitative phase imaging in biomedicine. *Nat.*
537 *Photonics* **12**, 578–589 (2018).
- 538 12. R. Barer, Interference Microscopy and Mass Determination. *Nature* **169**, 366–367
539 (1952).
- 540 13. G. Popescu, *et al.*, Optical imaging of cell mass and growth dynamics. *Am. J. Physiol.*
541 *Physiol.* **295**, C538–C544 (2008).

- 542 14. K. Kim, *et al.*, Optical diffraction tomography techniques for the study of cell
543 pathophysiology. *J. Biomed. Photonics Eng.* **2**, 020201 (2016).
- 544 15. D. Midtvedt, E. Olsén, F. Höök, G. D. M. Jeffries, Label-free spatio-temporal monitoring
545 of cytosolic mass, osmolarity, and volume in living cells. *Nat. Commun.* **10**, 340 (2019).
- 546 16. H. Zhao, P. H. Brown, P. Schuck, On the Distribution of Protein Refractive Index
547 Increments. *Biophys. J.* **100**, 2309–2317 (2011).
- 548 17. T. A. Zangle, M. A. Teitell, Live-cell mass profiling: An emerging approach in
549 quantitative biophysics. *Nat. Methods* **11**, 1221–1228 (2014).
- 550 18. P. Y. Liu, *et al.*, Cell Refractive Index for Cell Biology and Disease Diagnosis: Past,
551 Present and Future. *Lab Chip* **16**, 634–644 (2015).
- 552 19. J. Aizenberg, V. C. Sundar, A. D. Yablon, J. C. Weaver, G. Chen, Biological glass fibers:
553 Correlation between optical and structural properties. *Proc. Natl. Acad. Sci.* **101**, 3358–
554 3363 (2004).
- 555 20. J. M. Soto, J. A. Rodrigo, T. Alieva, Label-free quantitative 3D tomographic imaging
556 for partially coherent light microscopy. *Opt. Express* **25**, 15699–15712 (2017).
- 557 21. N. Otsu, A Threshold Selection Method from Gray-Level Histograms. *IEEE Trans. Syst.*
558 *Man. Cybern.* **9**, 62–66 (1979).
- 559 22. W. Choi, *et al.*, Tomographic phase microscopy. *Nat. Methods* **4**, 717–719 (2007).
- 560 23. S. Chowdhury, *et al.*, High-resolution 3D refractive index microscopy of multiple-
561 scattering samples from intensity images. *Optica* **6**, 1211–1219 (2019).
- 562 24. S. Penkov, *et al.*, A metabolic switch regulates the transition between growth and
563 diapause in *C. elegans*. *BMC Biol.* **18**, 31 (2020).
- 564 25. V. Ntziachristos, Going deeper than microscopy: The optical imaging frontier in biology.
565 *Nat. Methods* **7**, 603–614 (2010).
- 566 26. J. Lim, A. B. Ayoub, E. E. Antoine, D. Psaltis, High-fidelity optical diffraction
567 tomography of multiple scattering samples. *Light Sci. Appl.* **8**, 82 (2019).

- 568 27. D. Gems, *et al.*, Two pleiotropic classes of *daf-2* mutation affect larval arrest, adult
569 behavior, reproduction and longevity in *Caenorhabditis elegans*. *Genetics* **150**, 129–155
570 (1998).
- 571 28. P. Narbonne, R. Roy, *Caenorhabditis elegans* dauers need LKB1/AMPK to ration lipid
572 reserves and ensure long-term survival. *Nature* **457**, 210–214 (2009).
- 573 29. K. Nishizawa, *et al.*, Universal glass-forming behavior of in vitro and living cytoplasm.
574 *Sci. Rep.* **7**, 15143 (2017).
- 575 30. T. C. Boothby, *et al.*, Tardigrades Use Intrinsically Disordered Proteins to Survive
576 Desiccation. *Mol. Cell* **65**, 975-984.e5 (2017).
- 577 31. S. Möllmert, *et al.*, Zebrafish Spinal Cord Repair Is Accompanied by Transient Tissue
578 Stiffening. *Biophys. J.* **118**, 448–463 (2020).
- 579 32. G. Scarcelli, *et al.*, Noncontact three-dimensional mapping of intracellular
580 hydromechanical properties by Brillouin microscopy. *Nat. Methods* **12**, 1132–1134
581 (2015).
- 582 33. R. Schlüßler, *et al.*, Mechanical Mapping of Spinal Cord Growth and Repair in Living
583 Zebrafish Larvae by Brillouin Imaging. *Biophys. J.* **115**, 911–923 (2018).
- 584 34. I. Remer, R. Shaashoua, N. Shemesh, A. Ben-Zvi, A. Bilenca, High-sensitivity and high-
585 specificity biomechanical imaging by stimulated Brillouin scattering microscopy. *Nat.*
586 *Methods* **17**, 913–916 (2020).
- 587 35. R. Schlüßler, *et al.*, Combined fluorescence, optical diffraction tomography and
588 Brillouin microscopy. *bioRxiv*, 2020.10.30.361808 (2020).
- 589 36. L. Ma, *et al.*, Phase correlation imaging of unlabeled cell dynamics. *Sci. Rep.* **6**, 32702
590 (2016).
- 591 37. M. Drechsler, F. Giavazzi, R. Cerbino, I. M. Palacios, Active diffusion and advection in
592 *Drosophila* oocytes result from the interplay of actin and microtubules. *Nat. Commun.* **8**
593 (2017).

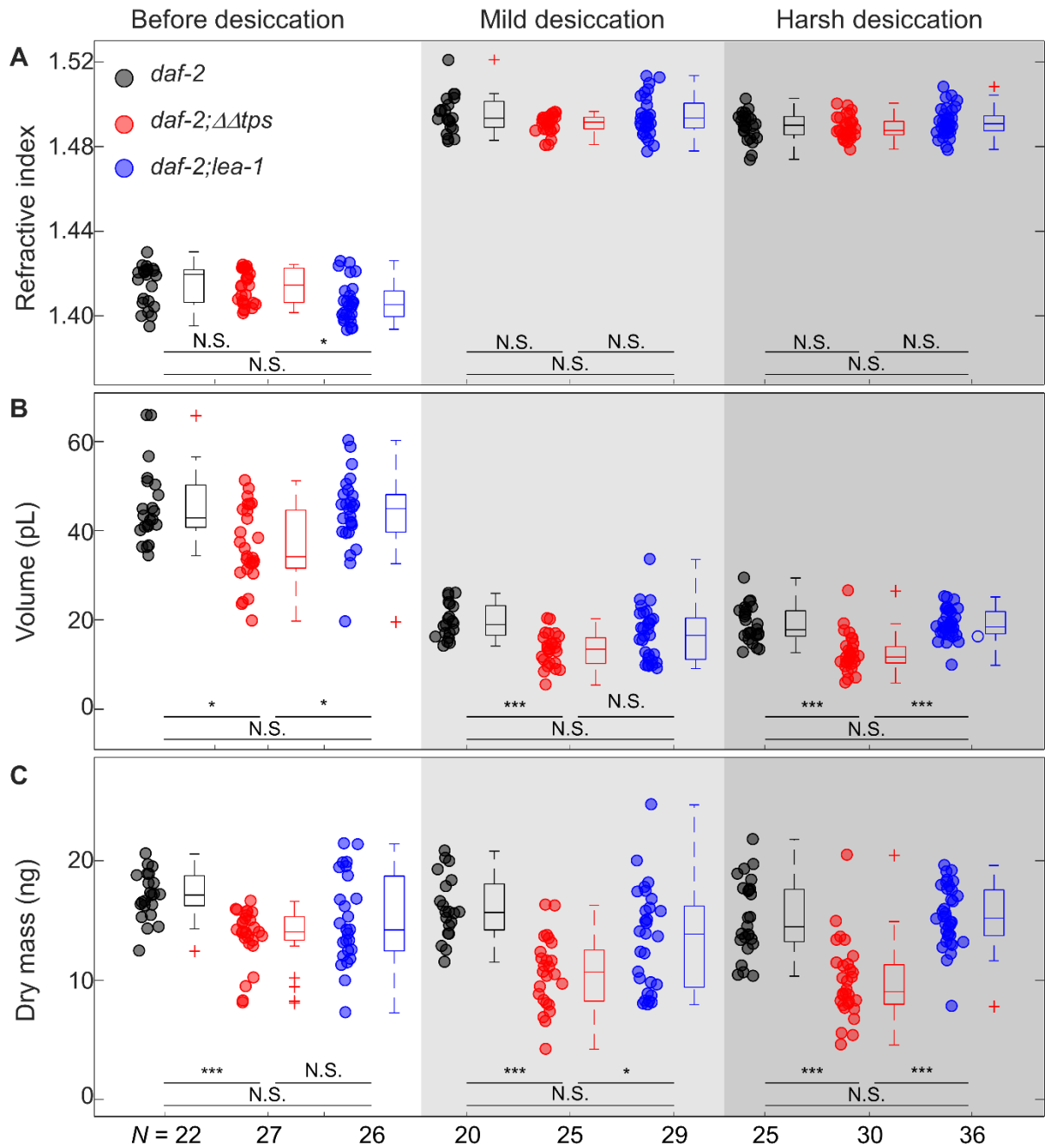
- 594 38. S. Chakrabortee, *et al.*, Hydrophilic protein associated with desiccation tolerance
595 exhibits broad protein stabilization function. *Proc. Natl. Acad. Sci.* **104**, 18073–18078
596 (2007).
- 597 39. S. Chakrabortee, *et al.*, Intrinsically disordered proteins as molecular shields. *Mol.*
598 *Biosyst.* **8**, 210–219 (2012).
- 599 40. S. Abuhattum, *et al.*, Intracellular Mass Density Increase Is Accompanying but Not
600 Sufficient for Stiffening and Growth Arrest of Yeast Cells. *Front. Phys.* **6**, 131 (2018).
- 601 41. E. Cuche, P. Marquet, C. Depeursinge, Spatial filtering for zero-order and twin-image
602 elimination in digital off-axis holography. *Appl. Opt.* **39**, 4070–4075 (2000).
- 603 42. E. Wolf, Three-dimensional structure determination of semi-transparent objects from
604 holographic data. *Opt. Commun.* **1**, 153–156 (1969).
- 605 43. K. Kim, *et al.*, High-resolution three-dimensional imaging of red blood cells parasitized
606 by *Plasmodium falciparum* and in situ hemozoin crystals using optical diffraction
607 tomography. *J. Biomed. Opt.* **19**, 011005 (2014).
- 608 44. K. Kim, J. Guck, The Relative Densities of Cytoplasm and Nuclear Compartments Are
609 Robust against Strong Perturbation. *Biophys. J.* **119**, 1946–1957 (2020).

610 **Supplementary Figures**



611

612 **Supplementary Figure 1.** Correlation between refractive index (RI) tomograms and epi-
613 fluorescence images of lipid droplets in dauer larvae. (A) Central cross-sectional slice through
614 an RI tomogram of a typical dauer larva. Color scale shows RI. (B) Epi-fluorescence image of
615 the same dauer larva in which the lipid content is stained with Nile Red. (C) Mean RI of dauer
616 larvae at the L3 stage, as well as of lipid droplets and non-lipid regions in the Nile Red-stained
617 dauer larvae. The numbers of L3 and dauer larvae measured are $N = 25$ and 20, respectively.

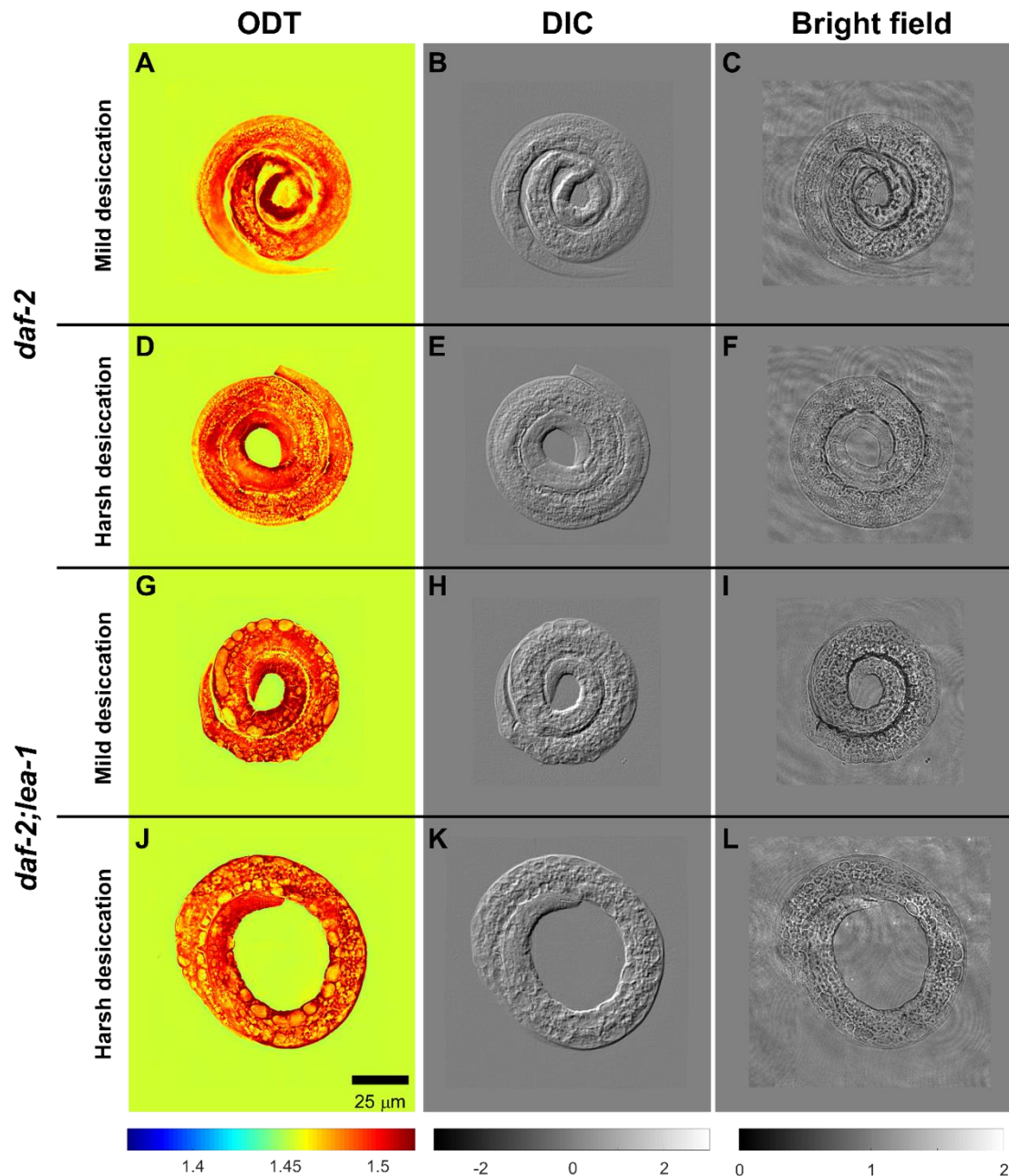


618

619 **Supplementary Figure 2.** Quantitative characterization of wild type (black), trehalose deletion

620 mutant (red), and LEA-1 deletion mutant (blue) dauer larvae in different conditions. (A) The

621 mean refractive index, (B) volume, and (C) dry mass of the dauer larvae.



622

623 **Supplementary Figure 3.** Comparison of images acquired by different microscopy modalities.

624 (A, D, G, J) Typical central cross-sectional slices through RI tomograms, (B, E, H, K) emulated

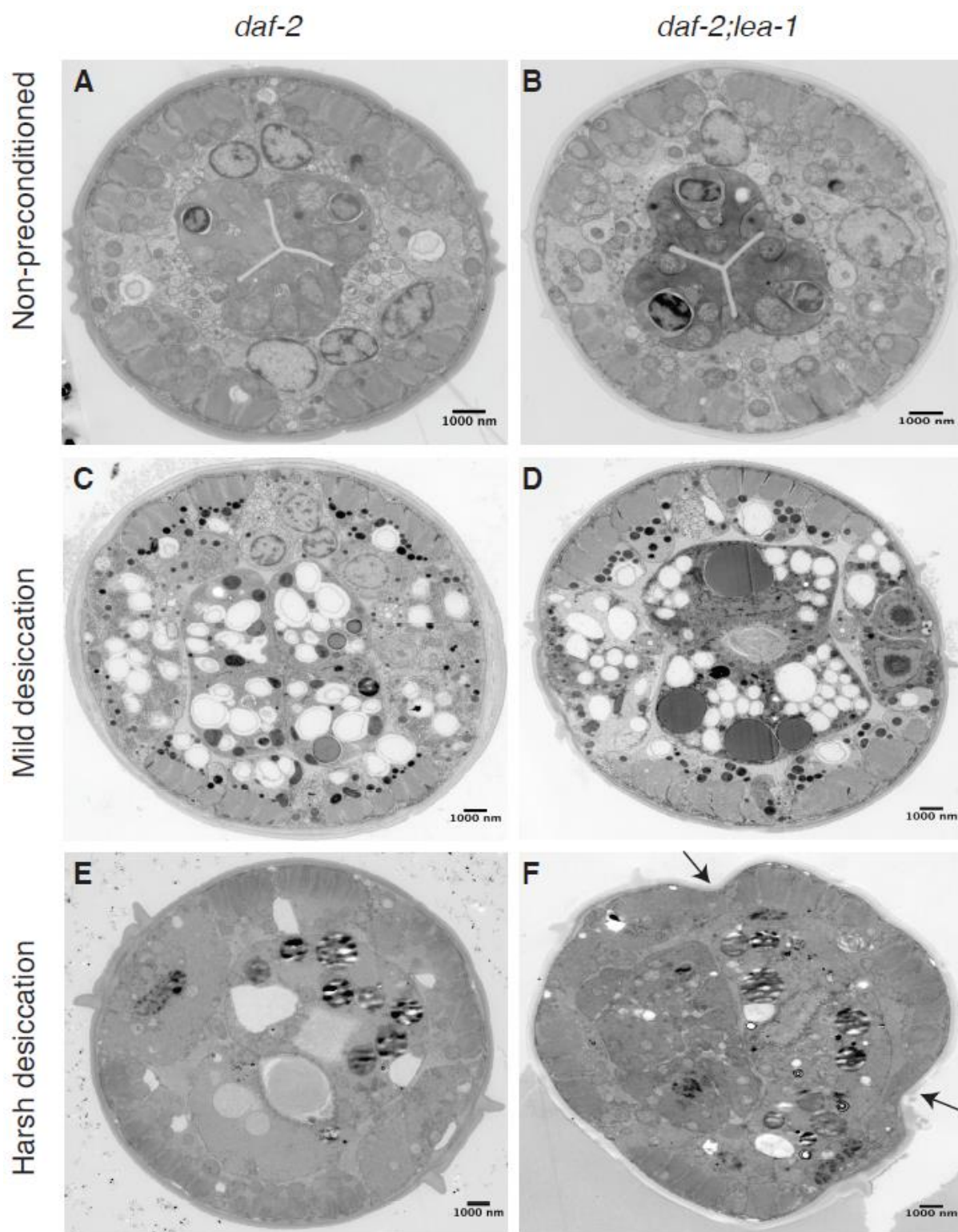
625 differential interference contrast (DIC) images, and (C, F, I, L) bright field images of *C. elegans*

626 dauer larvae. (A – C) represent wild type after mild (98% RH) desiccation, (D – F) wild type

627 after harsh (60% RH) desiccation, (G – I) *lea-1* deletion mutants *daf-2;lea-1* after mild

628 desiccation, and (J – L) *daf-2;lea-1* after harsh desiccation. Color scale shows RI. Grey scales

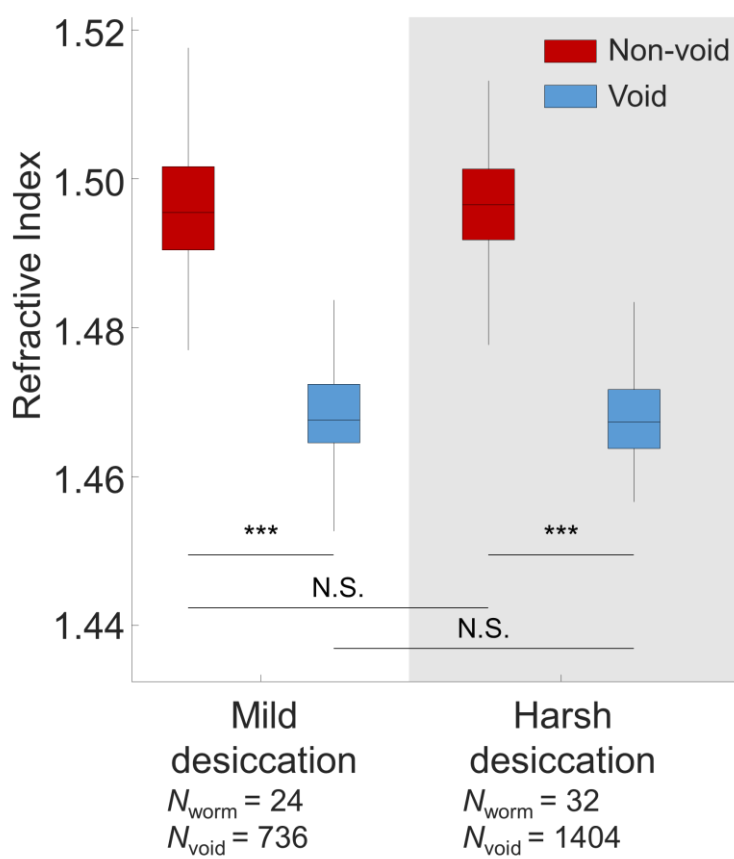
629 show light intensity in the arbitrary unit.



630

631 **Supplementary Figure 4.** Electron micrographs of (A, C, E) wild type (*daf-2*) and (B, D, F)
632 *lea-1* deletion mutant (*daf-2;lea-1*) in (A, B) the non-preconditioned, (C, D) mild desiccation,
633 and (E, F) harsh desiccation conditions. The arrows in F indicate the shrinkage of the desiccated
634 dauer larvae of *lea-1* deletion mutant.

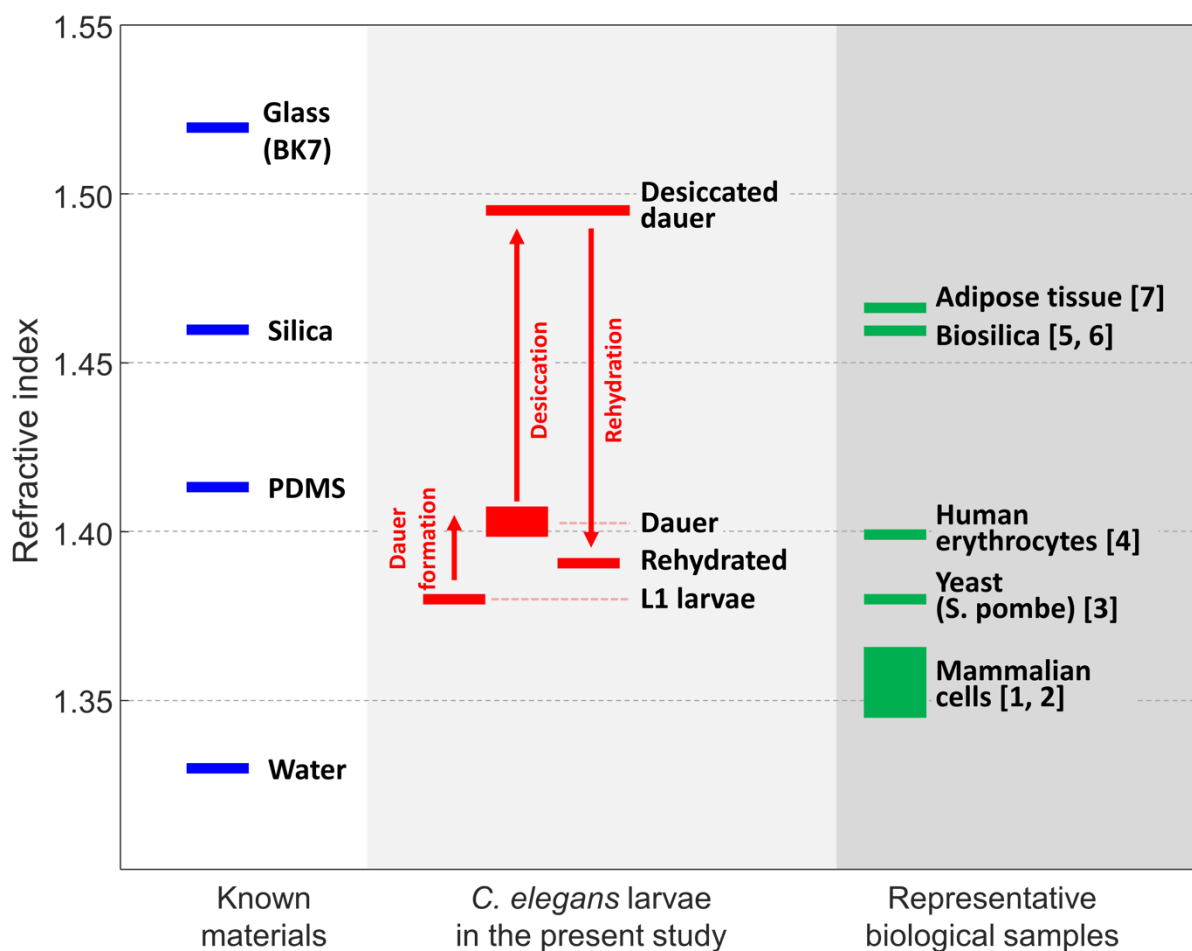
635



636

637 **Supplementary Figure 5.** Refractive index in void regions and their periphery of *lea-1* deletion

638 mutant during mild and harsh desiccation conditions.



639

640 **Supplementary Figure 6.** Graphical summary on the measured refractive index (RI) value of
641 *C. elegans* larvae in the present study (center) compared to the RI of known inanimate materials
642 (left) and representative biological samples (right).

643 **Supplementary Information**

644 **Supplementary Video 1.** Visualization of the RI tomogram and rendered isosurface of a typical

645 *C. elegans* larva at the L3 stage.

646 **Supplementary Video 2.** Visualization of the RI tomogram and rendered isosurface of a typical

647 *C. elegans* dauer larva of controls after harsh desiccation (60% RH).

648 **Supplementary Video 3.** Visualization of the RI tomogram and rendered isosurface of a typical

649 *C. elegans* dauer larva of trehalose deletion mutants *daf-2;ΔΔtps* after harsh desiccation (60%

650 RH).

651 **Supplementary Video 4.** Visualization of the RI tomogram and rendered isosurface of a typical

652 *C. elegans* larva of *lea-1* deletion mutants *daf-2;lea-1* after harsh desiccation (60% RH).

653

654 **Supplementary References**

655 1. P. Y. Liu, et al., Cell Refractive Index for Cell Biology and Disease Diagnosis: Past,
656 Present and Future. *Lab Chip* **16**, 634–644 (2015).

657 2. M. Schürmann, et al., Three-dimensional correlative single-cell imaging utilizing
658 fluorescence and refractive index tomography. *J. Biophotonics* **11**, e201700145 (2018).

659 3. S. Abuhattum, et al., Intracellular Mass Density Increase Is Accompanying but Not
660 Sufficient for Stiffening and Growth Arrest of Yeast Cells. *Front. Phys.* **6**, 131 (2018).

661 4. Y. Park, et al., Refractive index maps and membrane dynamics of human red blood cells
662 parasitized by Plasmodium falciparum. *Proc. Natl. Acad. Sci.* **105**, 13730–13735 (2008).

663 5. J. Aizenberg, V. C. Sundar, A. D. Yablon, J. C. Weaver, G. Chen, Biological glass
664 fibers: Correlation between optical and structural properties. *Proc. Natl. Acad. Sci.* **101**, 3358–
665 3363 (2004).

666 6. J. M. Soto, J. A. Rodrigo, T. Alieva, Label-free quantitative 3D tomographic imaging
667 for partially coherent light microscopy. *Opt. Express* **25**, 15699–15712 (2017).

- 668 7. I. Y. Yanina, E. N. Lazareva, V. V. Tuchin, Refractive index of adipose tissue and lipid
669 droplet measured in wide spectral and temperature ranges. *Appl. Opt.* **57**, 4839–4848 (2018).